Multi-Target Beamforming Optimization for Fluid Antenna-Enabled Multi-Static ISAC

Xingliang Lou, Student Member, IEEE, Wenchao Xia, Member, IEEE, Yongxu Zhu, Senior Member, IEEE, Kai-Kit Wong, Fellow, IEEE, and Chan-Byoung Chae, Fellow, IEEE

Abstract—This study investigates a fluid antenna (FA)-enabled multi-static integrated sensing and communication (ISAC) system. Within this system, multiple transmit access points (TAPs) are employed to transmit ISAC signals, enabling simultaneous downlink communication and target sensing. At the same time, there is a receive access point (RAP) to capture the reflected sensing signals for target detection. All of the TAPs are equipped with FAs to leverage the spatial degree of freedom. We formulate a maximization problem of the worst-case detection probability of designated targets subject to the communication constraints of the users, to optimize both the beamforming matrix and antenna position vector (APV) of each TAP. To address the nonconvexity of the problem, we use an alternating optimization approach over two subproblems: (1) beamforming optimization, and (2) optimization of APVs. For the first subproblem, we use the semi-definite relaxation (SDR) method to derive the optimal beamforming vectors given fixed APVs. Then the latter is solved by the second-order Taylor series expansion to approximate the function related to the APVs in a convex form. Simulation results demonstrate that the adoption of FA significantly enhances the sensing performance of our proposed system. Also, the proposed cooperative multi-static ISAC system coordinates communication and sensing tasks across various TAPs effectively, underscoring its potential for improving overall system performance.

Index Terms—Fluid antenna system (FAS), integrated sensing and communication (ISAC), antenna position vector optimization, beamforming matrix optimization.

I. INTRODUCTION

ITH the rapid advances paving the way for the sixth generation (6G), communication systems are evolving into sophisticated networks designed to deliver ubiquitous and intelligent connectivity for all devices and applications [1], [2]. This progression aims to enable seamless, smart interactions across a wide range of technologies and industries, fostering an era of pervasive intelligence. The emergence of technologies, such as connected autonomous vehicles (CAVs) and unmanned aerial vehicles (UAVs), means that 6G systems not only meet the increased demand for data throughput and reliability but also fulfil stringent requirements for low-latency communications and high-precision sensing. However, employing diverse

X. Lou and W. Xia are with the Jiangsu Key Laboratory of Wireless Communications, and also with the Engineering Research Center of Health Service System Based on Ubiquitous Wireless Networks, Ministry of Education, Nanjing University of Posts and Telecommunications, Nanjing 210003, China (e-mail: 2022010109@njupt.edu.cn, xiawenchao@njupt.edu.cn).

Y. Zhu is with the National Communications Research Laboratory, Southeast University, Nanjing 210096, China (e-mail: yongxu.zhu@seu.edu.cn).

K. K. Wong is with the Department of Electronic and Electrical Engineering, University College London, London WC1E 7JE, United Kingdom, and he is also affiliated with Yonsei Frontier Laboratory, Yonsei University, Seoul, 03722, Republic of Korea (e-mail: kai-kit.wong@ucl.ac.uk).

C. B. Chae is with School of Integrated Technology, Yonsei University, Seoul, 03722, Republic of Korea (e-mail: cbchae@yonsei.ac.kr).

software and hardware platforms and spectrum resources for both communication and sensing poses additional challenges to the already constrained network resources. Fortunately, recent advancements in multiple-input multiple-output (MIMO) technology [3], [4] indicate that high-resolution sensing can be accomplished by utilizing communication signals [5]. This approach offers a promising solution for enhancing sensing accuracy without necessitating additional spectrum resources or complex hardware. As a consequence, it is feasible to design integrated wireless networks capable of simultaneously performing both communication and sensing tasks, i.e., integrated sensing and communication (ISAC) [6]. The core principle of ISAC is predicated on the shared utilization of hardware platforms and signal processing modules to efficiently execute both communication and sensing operations [7].

In recent years, much progress has been made for ISAC, particularly in areas such as waveform design and signal processing. Notably, [8] investigated the interaction between the downlink base station (BS) and MIMO radar in a coexisting system, proposing two approaches for achieving simultaneous sensing and communication. One approach involves utilizing distinct antenna arrays designed with a null-space technique for sensing signals. Another approach is to employ a shared waveform, which has garnered broader acceptance due to its efficiency and practicality. Building on these advancements, a joint transmission model was developed in [9], [10]. This model enables simultaneous beam steering toward both targets and users by transmitting an integrated signal combining sensing and data transmission waveforms. Moreover, the authors of [11] enhanced the sensing performance of ISAC system by jointly optimizing parameters such as beamforming and the duration of non-orthogonal multiple access transmission.

To mitigate sensing uncertainties arising from fading and interference in mono-static ISAC systems, multi-static ISAC systems have attracted significant interest. These systems enhance robustness against environmental variations and improve overall system reliability through coordinated deployment of multiple access points. For instance, [12] introduced a multistatic architecture where users serve as uplink sensing points, thereby augmenting the downlink detection capabilities of the BS. To fully exploit these advantages, recent studies such as [13], [14], [15], [16] elaborated on two key mechanisms: transmit access points (TAPs) transmitting ISAC signals for both communication and target detection, and receive access points (RAPs) capturing the reflected signals that are subsequently processed by a central controller (CC). Furthermore, [17] proposed a multi-static ISAC system oriented towards edge intelligence, which minimized the overall power consumption by jointly optimizing sensing beamforming, offloading transmission beamforming, and multi-station sensing scheduling.

However, in conventional ISAC systems, fixed-position antennas are used for both sensing and communication tasks. Although beamforming matrix optimization can enhance either sensing or communication performance, the spatial rigidity of static antenna deployments restricts their ability to harness available degrees of freedom (DoFs) across continuous spatial ranges, resulting in suboptimal spatial diversity [18]. Also, these fixed-position antennas greatly limit sensing resolution, as this performance heavily depends on the geometric configuration of the antenna array. Consequently, it is essential to explore antenna position vector (APV) optimization techniques to enhance the spatial diversity within wireless channels. Fluid antenna (FA) systems [19], [20], [21], [22], sometimes referred to as movable antenna (MA) systems [23], provide a viable solution by providing additional DoFs in beamforming through dynamic APV [24], [25], [26]. By enabling dynamic antenna repositioning within predefined regions utilizing technologies such as [27], [28], [29], [30], FA systems imitate having many distributed antennas over a given space, fully utilizing the entire spatial region. This results in higher angular resolution without the need for additional antenna elements, thereby maximizing cost-effectiveness and performance.

FA systems not only show significant potential for wireless communication systems, but also can play an important role in enhancing ISAC capabilities. The authors of [31] summarized the advantages of FA-enabled ISAC systems, including enhanced spectral efficiency, flexible and precise beamforming, and adjustable signal coverage ranges. Moreover, [31] investigated the problem of minimizing the total transmit power in an FA-enabled full-duplex ISAC system, where the BS is equipped with both a receiving FA and a transmitting FA. Concurrently, [32], [33], [34] introduced an FA-enabled ISAC framework that simultaneously optimizes the transmit beamforming matrix and port selection by reconfiguring FA positions across predefined ports, thereby maximizing spatial diversity gains for dual-functional performance enhancement. Later, [35] studied a dual-FA architecture where both BS and users are equipped with FA, and jointly optimized the transmit beamforming matrix and APV to maximize communication rates while meeting the sensing beampattern gain and transmission power requirements of the BS. The integration of FA with other emerging paradigms further expands ISAC capabilities. For example, [36] developed an ISAC system augmented by both FA and reconfigurable intelligent surfaces (RIS), which overcomes coverage limitations in non-line-ofsight (NLOS) environments through joint optimization of the beamforming matrix at the BS, the reflection coefficients on the RIS, and the APV. Additionally, [37] proposed a deep reinforcement learning framework to address the non-convex problem of jointly optimizing the beamforming matrix and APV, establishing an end-to-end learning architecture that circumvents the limitations of traditional convex relaxation methods.

However, while existing studies [12], [13], [14], [15], [16], [17] on fixed-position antenna multi-static ISAC systems achieved cooperative sensing, there rigid antenna configurations prevented dynamic reconfiguration of the sensing ge-

ometry. Although emerging FA-enabled ISAC systems [31], [32], [33], [34], [35], [36], [37] enhanced dual-functional performance by optimizing antenna positions, current approaches primarily focused on single-target detection scenarios and implemented FAs at a single TAP, failing to exploit the multi-target detection capacity of FA-enabled multi-static ISAC systems. Consequently, two critical challenges remain unaddressed: the scalability of sensing optimization for multi-target scenarios and the coordination across distributed TAPs.

Building on the discussion above, we focus on designing optimal solutions and efficient algorithms for the FA-enabled multi-static ISAC system where multiple TAPs collaboratively transmit dual-functional ISAC signals to simultaneously execute joint downlink communication and multi-target sensing operations. At the same time, a RAP captures the reflected sensing signals for multi-target detection. Moreover, we adopt the full synchronization framework between RAP and TAPs described in [38]. This synchronization paradigm, also used in [39], constitutes the fundamental operational prerequisite for our cross-node cooperative processing framework. Additionally, Table I presents a comparative analysis of existing methods and our proposed solution.

The key contributions of this work are threefold:

- Firstly, to address the limitations of conventional multistatic ISAC systems, particularly the restricted spatial DoFs and limited beamforming flexibility caused by fixedposition antennas, which significantly constrain sensing resolution in multi-target scenarios, we propose equipping all TAPs with FA technology. This approach enables continuous reconfiguration of antenna positions within a predefined one-dimensional (1D) linear domain, thereby allowing for dynamic optimization of APVs to adapt varying channel conditions and geometric constraints. Moreover, the introduction of FA technology effectively addresses the issue of angle ambiguity that arises in multi-target sensing with fixed-position antennas, thereby achieving higher-resolution sensing performance. By leveraging the continuous position tunability offered by FAs, we can achieve narrower beamwidths and more focused energy steering toward multi-target simultaneously.
- Secondly, to reconcile the competing demands of multiuser communication and multi-target detection, we construct an optimization problem that co-optimizes two critical design parameters: transmit beamforming matrices and APVs. Our aim is to maximize the worst-case detection probability for designated targets, constrained by a signal-to-interference-plus-noise ratio (SINR) threshold for all users, the power budget at each TAP, and the APVs boundaries. However, the APV optimization is a challenging problem, which arises from nonlinear dependence on communication channels and steering vectors of targets relative to the APVs, and the strong coupling between the beamforming matrices and APVs. Therefore, we propose a two-stage alternating optimization (AO) algorithm that decouples the joint design into sequential subproblems. In the first stage, the beamforming subproblem leverages semi-definite relaxation (SDR) to simultaneously address SINR constraints and maximize multi-target detection

TABLE I
COMPARATIVE ANALYSIS OF EXISTING METHODS AND PROPOSED SOLUTION

Category	Key Contributions	Limitations vs. Our Work
Fixed-Position Antenna Multi-Static	Cooperative sensing-communication,	Unable to reconfigure antenna
ISAC [12], [13], [14], [15], [16], [17]	multi-node joint beamforming	dynamically, limited angular resolution for close-spaced targets
FA-Enabled Communication	FA-enabled DoF for MIMO	No ISAC integration: focus
[24], [25], [26], [27], [28], [29], [30]	capacity, APV algorithms	solely on communication
Single-Node FA-Enabled ISAC	Joint sensing-communication	Multi-target sensing unsupported,
[31], [32], [33], [34], [35], [36], [37]	tradeoff, enhance performance via FA	no multi-TAP coordination

probability under fixed APVs; In the second stage, the APVs subproblem employs a novel second-order Taylor approximation to convexify the highly non-convex, position-dependent steering vector expressions that arise from multi-TAP coordination given fixed beamforming matrices. This approach enables simultaneous multi-target sensing and multi-user communication.

Finally, we present simulation results evaluating the sensing performance gains of the proposed system. Through comparative analysis with the conventional fixed-position antenna ISAC baseline under diverse scenarios, the numerical results demonstrate that the FA-enabled architecture significantly improves the sensing performance compared to fixed-position antenna architectures, validating the superiority of dynamic APV optimization. Specifically, simulation results demonstrate that FA-enabled system with M=12 antennas outperform fixed-position systems with M=16 antennas. Moreover, in the case of closely spaced targets, only the FA-enabled system successfully resolves both targets, whereas fixed-position antenna system fails to distinguish them. Furthermore, it is evident that the cooperative beamforming framework achieves sensing-communication resource utilization efficiency, demonstrating effective cross-functional task coordination among distributed TAPs.

The remaining content is organized as follows. Section II introduces the system model of the considered framework. Then Section III develops the AO algorithm for joint beamforming design and APV coordination, discusses its convergence properties and also provides computational complexity analysis. Simulation results are presented and analyzed in Section IV, offering insights into the efficacy of the proposed approaches. Finally, Section V concludes this paper.

Notation: Matrices and vectors are represented using bold-face uppercase symbols (e.g., \mathbf{B}), and boldface lowercase symbols (e.g., \mathbf{b}), respectively. Statistical expectation is denoted by $\mathbb{E}(\cdot)$. The operator diag (\cdot) generates a diagonal matrix from its vector argument. The l_1 and l_2 norms of a vector are indicated by $\|\cdot\|_1$ and $\|\cdot\|_2$, respectively. Furthermore, $|\cdot|$ and \angle denote the magnitude and phase of a complex number, respectively. The trace operation is denoted by $\operatorname{tr}(\cdot)$. The superscripts $(\cdot)^T$ and $(\cdot)^H$ indicate the transpose and Hermitian transpose operations for matrices, respectively. The identity matrix is represented by \mathbf{I} . The function $\operatorname{rank}(\mathbf{M})$ indicates the rank of matrix \mathbf{M} . The notation $\mathbf{M} \succeq 0$ denotes

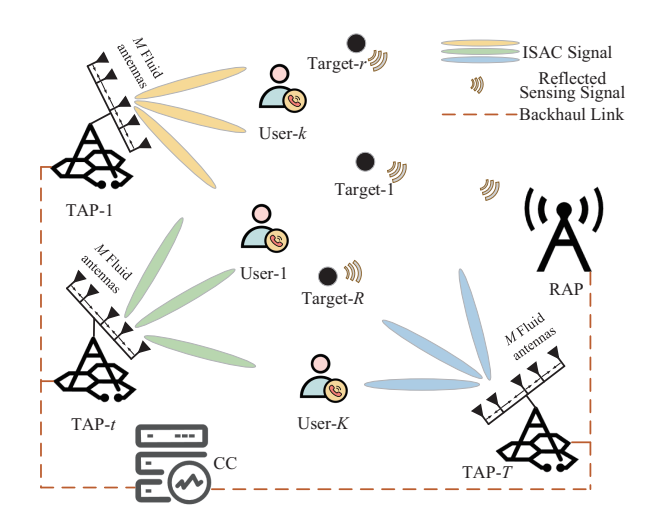


Fig. 1. The FA-enabled multi-static ISAC system architecture.

that the matrix M is positive semi-definite.

II. SYSTEM MODEL

A. System Setting

Consider a downlink transmission scenario implemented in an FA-enabled multi-static ISAC system, whose architecture is illustrated in Fig. 1. The proposed system is composed of T TAPs, each equipped with M FAs, and a RAP equipped with N fixed-position receive antennas specifically designed for capturing the reflected signals from sensing targets. This integrated framework is designed to simultaneously detect R point-like targets, while guaranteeing communication service to K users with single-antenna. We represent the sets of TAPs, targets, and users with $\mathcal{T} = \{1, \dots, T\}, \mathcal{R} = \{1, \dots, R\},$ and $\mathcal{K} = \{1, \dots, K\}$, respectively. Each FA module exhibits continuous mobility along a predefined 1D linear track of length D during operation. Adopting a two-dimensional (2D) coordinate system, the positions of the t-th TAP, the RAP, and the r-th target are given by $\mathbf{c}_{1,t} = (x_{1,t}, y_{1,t}),$ $\mathbf{c}_0=(x_0,y_0)$, and $\mathbf{c}_{2,r}=(x_{2,r},y_{2,r})$, respectively. We define $p_{t,m} \in [0,D]$ as the position of the m-th FA in the t-th TAP. The complete spatial configuration is encapsulated in the APV $\mathbf{p}_{t} = [p_{t,1}, p_{t,2}, \dots, p_{t,M}],$ to be optimized.

Define $\mathbf{s}[l] = [s_1[l], \dots, s_K[l]]^T \in \mathbb{C}^{K \times 1}, l \in L$ as the information-bearing signals for all K users over L transmission blocks, where $l \in \{1, \dots, L\}$ indexes the communication

time slots. These signals satisfy the normalized power constraint $\frac{1}{L}\mathbb{E}\left(\mathbf{s}\mathbf{s}^{H}\right) = \mathbf{I}$. To guarantee sufficient spatial DoFs for multi-user beamforming, we impose the constraint that the number of antennas per TAP should not be less than the number of users, i.e., $M \geq K$ [40]. Given that TAPs are interconnected via backhaul links, the signal vector $\mathbf{s}[l]$ can be reliably shared across all the TAPs and the RAP prior to transmission. However, the signal vector remains unknown a priori to the users. Building upon the key insight from [41], it is observed that introducing dedicated sensing signals leads to their vanishing contribution in the optimal solution due to mutual interference under the considered system constraints. As such, our framework strategically omits dedicated sensing signals and exploits solely the information-bearing waveforms for joint sensing and communication operations. This design philosophy fully harnesses the inherent dual utility of ISAC that simultaneously achieves both communication and sensing without requiring additional spectral resources or signaling overhead.

Let $\mathbf{W}_t = [\mathbf{w}_{t,1}, \mathbf{w}_{t,2}, \dots, \mathbf{w}_{t,K}] \in \mathbb{C}^{M \times K}$ be the transmit beamforming matrix at the t-th TAP, where each column vector $\mathbf{w}_{t,k}$ denotes the adaptive beamforming coefficients allocated to the k-th user. Under this configuration, the ISAC signal of the t-th TAP after beamforming is formulated as

$$\mathbf{X}_{t}[l] = \sum_{k=1}^{K} \mathbf{w}_{t,k} s_{k}[l] = \mathbf{W}_{t} \mathbf{s}[l] \in \mathbb{C}^{M \times 1}.$$
 (1)

The transmit power at each TAP is constrained by

$$\|\mathbf{X}_t[l]\|^2 = \operatorname{tr}\left(\mathbf{W}_t\mathbf{W}_t^H\right) \le P_t, \ t \in \mathcal{T},$$
 (2)

with P_t the maximum transmit power for the t-th TAP.

B. Communication Model

Using a geometric line-of-sight (LoS) propagation model¹, the channel vector between the t-th TAP and the k-th user is formulated as

$$\mathbf{h}_{t,k} = \varrho_{t,k} \mathbf{a}_1 \left(\mathbf{p}_t, \theta_{t,k} \right) \in \mathbb{C}^{M \times 1}, \tag{3}$$

where $\varrho_{t,k}$ represents the channel propagation gain, and $\theta_{t,k}$ denotes the azimuth angle of the k-th user relative to the antenna array at the t-th TAP. The steering vector \mathbf{a}_1 (\mathbf{p}_t, \star), which characterizes transmit steering vector, is defined as

$$\mathbf{a}_{1}(\mathbf{p}_{t},\star) = \left[e^{j\frac{2\pi}{\lambda}p_{t,1}\sin(\star)}, \dots, e^{j\frac{2\pi}{\lambda}p_{t,M}\sin(\star)}\right]^{T} \in \mathbb{C}^{M\times 1}, \quad (4)$$

with λ standing for the carrier wavelength.

Then the received signal at the k-th user is composed of

three distinct components, given by

$$y_{k}[l] = \sum_{t=1}^{T} \mathbf{h}_{t,k}^{H} \mathbf{w}_{t,k} s_{k}[l] + \sum_{t=1}^{T} \sum_{\substack{k'=1\\k' \neq k}}^{K} \mathbf{h}_{t,k}^{H} \mathbf{w}_{t,k'} s_{k'}[l] + \mathbf{n}_{c}[l], \quad (5)$$

where $\mathbf{n}_{\rm c}\left[l\right]$ is the additive white Gaussian noise (AWGN), modeled as $\mathcal{CN}\left(0,\sigma_{\rm n}^2\right)$. The first term represents the desired signal component intended for the k-th user, incorporating contributions from all the TAPs. The second term accounts for the interference from the other users, which arises due to the superposition of signals intended for different users. Therefore, the SINR for the k-th user is derived as

$$\gamma_{k} = \frac{\sum_{t=1}^{T} \left| \mathbf{h}_{t,k}^{H} \mathbf{w}_{t,k} \right|^{2}}{\sum_{t=1}^{T} \sum_{k'=1 \atop k' \neq k}^{K} \left| \mathbf{h}_{t,k}^{H} \mathbf{w}_{t,k'} \right|^{2} + \sigma_{n}^{2}}.$$
 (6)

C. Sensing Model

The sensing channel gains for both the transmission link from the t-th TAP to the r-th target and the echo link from the r-th target to the RAP are given by

$$\alpha_{t,r} = \frac{\alpha}{\|\mathbf{c}_{1,t} - \mathbf{c}_{2,r}\|^2},\tag{7}$$

$$\alpha_r = \frac{\alpha}{\|\mathbf{c}_0 - \mathbf{c}_{2,r}\|^2},\tag{8}$$

where α denotes the reference channel power at 1 meter. By leveraging prior knowledge of the signals through backhaul links, the direct link between the t-th TAP and the RAP can be effectively canceled. Thus, the echo sensing signals of the RAP from the r-th target can be formulated as the superposition of the bi-static sensing links, which is given by

$$\mathbf{z}_{r}[l] = \sum_{t=1}^{T} \sqrt{\alpha_{t,r} \alpha_{r}} \beta_{t,r} \mathbf{a}_{2}(\phi_{r}) \mathbf{a}_{1}^{H}(\mathbf{p}_{t}, \varphi_{t,r}) \mathbf{W}_{t} \mathbf{s}[l] + \mathbf{n}_{s}[l], \quad (9)$$

where $\mathbf{n}_{\mathrm{s}} \sim \mathcal{CN}\left(\mathbf{0}, \sigma_{\mathrm{s}}^{2}\mathbf{I}_{N}\right)$ is the AWGN vector with variance σ_{s}^{2} , $\beta_{t,r}$ denotes the complex reflection coefficient of the r-th target, ϕ_{r} and $\varphi_{t,r}$ are the azimuth angles of the r-th target with respect to the RAP and the t-th TAP, respectively, and

$$\mathbf{a}_{2}(\star) = \left[1, \dots, e^{j(N-1)\frac{2\pi}{\lambda}d\sin(\star)}\right]^{T} \in \mathbb{C}^{N \times 1}$$
 (10)

is the receive steering vector with $d = \frac{\lambda}{2}$ spacing between adjacent uniform linear array (ULA) elements at the RAP.

D. FA Model

The antenna elements at the TAPs continuously move along predefined linear tracks. Depending on the implementation method, a minimum inter-element separation constraint may be enforced to mitigate the mutual coupling phenomenon between adjacent fluid antennas. These constraints can be

¹The LoS propagation model is adopted in this work, as ISAC systems commonly operate in high-frequency bands such as millimeter-wave, where the channel between the BS and the user is typically dominated by the LoS path [42]. Moreover, the LoS model can be extended to a more general field-response-based channel model that incorporates multiple propagation paths [43]. The optimization algorithms developed in this paper are also applicable to such generalized scenarios.

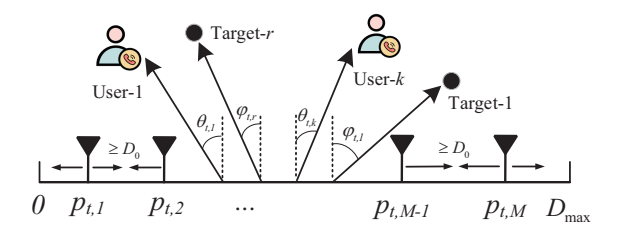


Fig. 2. The FA model for the t-th TAP.

mathematically expressed as

$$\mathbf{p}_{t} \in D, \ t \in \mathcal{T},$$
 $|p_{t,m} - p_{t,m-1}| \ge D_{0}, \ m = 2, 3, \dots, M, \ t \in \mathcal{T},$
(11)

where D_0 indicates the required minimum separation between neighboring antennas, and D represents the spatial range. The FA model at the t-th TAP is depicted in Fig. 2.

III. BEAMFORMING AND APV OPTIMIZATION

In this section, we establish a methodological framework for multi-target sensing optimization. First, we construct a maxmin problem to maximize the worst-case detection probability for specified sensing targets ² under the system constraints. Subsequently, we develop an AO algorithm, where the transmit beamforming matrices and APVs are iteratively optimized. Finally, analyses regarding convergence behavior and computational complexity are rigorously established.

A. Problem Formulation

We adopt the co-optimization of beamforming matrices and APVs with the aim of maximizing the worst-case detection probability $P_D\left(r\right)$ across all targets, while meeting the SINR constraints for the users, the power budget of the TAPs, and the physical constraints of the FAs, which is formulated as

$$P_{1}: \max_{\left\{\mathbf{W}_{t}, \mathbf{p}_{t}\right\}_{t \in \mathcal{T}}} \min_{r \in \mathcal{R}} P_{D}\left(r\right)$$
 (12a)

s.t.
$$\gamma_k \ge \Gamma, k \in \mathcal{K},$$
 (12b)

$$\operatorname{tr}\left(\mathbf{W}_{t}\mathbf{W}_{t}^{H}\right) \leq P_{t}, t \in \mathcal{T}, \tag{12c}$$

$$(11),$$

where Γ is the minimum SINR threshold for each user.

For the r-th potential target, the detection probability $P_{\rm D}\left(r\right)$ exhibits a monotonic relationship with the sensing signal-to-noise ratio (SNR) $\rho\left(r\right)$, as established in [14], [16]. The SNR for the r-th target is formulated as

$$\rho(r) = \sum_{t=1}^{T} \frac{LN\alpha^{2} |\beta_{t,r}|^{2} \mathbf{a}_{1}^{H} (\mathbf{p}_{t}, \varphi_{t,r}) \mathbf{W}_{t} \mathbf{W}_{t}^{H} \mathbf{a}_{1} (\mathbf{p}_{t}, \varphi_{t,r})}{\|\mathbf{c}_{1,t} - \mathbf{c}_{2,r}\|^{2} \|\mathbf{c}_{0} - \mathbf{c}_{2,r}\|^{2} \sigma_{s}^{2}}.$$
 (13)

²Upon receiving the signals, the RAP employs matched filters tuned to the unique propagation delay profiles in order to separate composite reflections from multiple TAPs. After spatial isolation through adaptive receive beamforming (Eq. (22) in [16]), the reflections corresponding to each target are combined. Joint target detection is then performed using a square law detector, as derived in Section IV of [16] through binary hypothesis testing.

Leveraging this monotonicity property, the original detection probability maximization can be equivalently transformed into SNR maximization.

Then by ignoring the constant scaling factor $\frac{LN\alpha^2}{\sigma_s^2}$, we obtain the simplified optimization problem, formulated as

$$P_{2}: \max_{\{\mathbf{W}_{t}, \mathbf{p}_{t}\}_{t \in \mathcal{T}}} \min_{r \in \mathcal{R}} \sum_{t=1}^{T} \zeta_{t,r} \mathbf{a}_{1}^{H} \left(\mathbf{p}_{t}, \varphi_{t,r}\right) \mathbf{W}_{t} \mathbf{W}_{t}^{H} \mathbf{a}_{1} \left(\mathbf{p}_{t}, \varphi_{t,r}\right)$$
s.t. (11), (12b), (12c),

where $\zeta_{t,r} = \frac{|\beta_{t,r}|^2}{\|\mathbf{c}_{1,t} - \mathbf{c}_{2,r}\|^2 \|\mathbf{c}_0 - \mathbf{c}_{2,r}\|^2}$ encapsulates the combined effects of target radar cross section (RCS) and bi-static range attenuation.

To facilitate optimization, we reformulate the problem P_2 through the introduction of an auxiliary variable ξ to homogenize the max-min objective, where the equivalent epigraph form is given by

$$P_3: \max_{\{\mathbf{W}_t, \mathbf{p}_t\}_{t \in \mathcal{T}}, \xi} \xi \tag{14a}$$

s.t.
$$\sum_{t=1}^{T} \zeta_{t,r} \mathbf{a}_{1}^{H} \left(\mathbf{p}_{t}, \varphi_{t,r} \right) \mathbf{W}_{t} \mathbf{W}_{t}^{H} \mathbf{a}_{1} \left(\mathbf{p}_{t}, \varphi_{t,r} \right) \geq \xi, r \in \mathcal{R}, \quad (14b)$$

$$(11), \quad (12b), \quad (12c).$$

The challenge in P_3 stems from the non-convex coupling between beamforming matrices $\{\mathbf{W}_t\}_{t\in\mathcal{T}}$ and APVs $\{\mathbf{p}_t\}_{t\in\mathcal{T}}$. To overcome this, we adopt an AO algorithm to iteratively address the problem P_3 , where each iteration updates a single variable subset while maintaining all other subsets fixed at their values obtained in the preceding iteration.

B. Updating Transmit Beamforming Matrix

The beamforming vectors $\{\mathbf{w}_{t,k}\}_{t\in\mathcal{T},k\in\mathcal{K}}$ involve inner products, resulting in a quadratic optimization problem. To tackle this computational complexity, we apply the SDR technique to convexify the formulation. Specifically, we construct auxiliary matrix variables as

$$\mathbf{V}_{t,k} = \mathbf{w}_{t,k} \mathbf{w}_{t,k}^{H}, \ t \in \mathcal{T}, k \in \mathcal{K}, \tag{15}$$

and reformulate the channel matrices as

$$\mathbf{H}_{t,k} = \mathbf{h}_{t,k} \mathbf{h}_{t,k}^{H}, \ t \in \mathcal{T}, k \in \mathcal{K}.$$
 (16)

Through this transformation, the SINR constraint for the k-th user can be rewritten as

$$\sum_{t=1}^{T} \operatorname{tr}\left(\mathbf{H}_{t,k} \mathbf{V}_{t,k}\right) - \sum_{t=1}^{T} \sum_{\substack{k'=1\\k' \neq k}}^{K} \Gamma \operatorname{tr}\left(\mathbf{H}_{t,k} \mathbf{V}_{t,k'}\right) \ge \Gamma \sigma_{n}^{2}. \quad (17)$$

Subsequently, by fixing the APVs and employing the SDR

technique, P_3 can be reformulated as

$$P_4: \max_{\{\mathbf{V}_{t,k} \succeq 0\}_{t \in \mathcal{T}, k \in \mathcal{K}}, \xi} \xi \tag{18a}$$

s.t.
$$\operatorname{tr}(\mathbf{V}_t) \le P_t, t \in \mathcal{T},$$
 (18b)

$$rank(\mathbf{V}_{t,k}) = 1, t \in \mathcal{T}, k \in \mathcal{K}, \tag{18c}$$

$$\sum_{t=1}^{T} \zeta_{t,r} \mathbf{a}_{1}^{H} \left(\mathbf{p}_{t}, \varphi_{t,r} \right) \mathbf{V}_{t} \mathbf{a}_{1} \left(\mathbf{p}_{t}, \varphi_{t,r} \right) \geq \xi, r \in \mathcal{R}, \quad (18d)$$
(17),

where $\mathbf{V}_t = \sum_{k=1}^K \mathbf{V}_{t,k}$. But due to the rank-1 constraints (18c), P_4 remains non-convex. To obtain a tractable convex approximation, P_4 is relaxed through dropping the rank-1 constraints on $\{\mathbf{V}_{t,k}\}_{t\in\mathcal{T},k\in\mathcal{K}}$, which gives

$$P_{5}: \max_{\{\mathbf{V}_{t,k} \succeq 0\}_{t \in \mathcal{T}, k \in \mathcal{K}}, \xi} \xi$$
s.t. (17), (18b), (18d).

This relaxed formulation constitutes a typical semi-definite program (SDP) problem that can be solved using convex optimization toolboxes, such as CVX [44].

Evidently, if the optimal solutions $\left\{\mathbf{V}_{t,k}^*\right\}_{t\in\mathcal{T},k\in\mathcal{K}}$ to problem P_5 satisfy the condition

$$\operatorname{rank}\left(\mathbf{V}_{t\,k}^{*}\right) = 1, t \in \mathcal{T}, k \in \mathcal{K},\tag{20}$$

those simultaneously attain optimality for P_4 . In the case where the rank-1 condition is not met, the Gaussian randomization methods [45] can be used to provide a rank-1 approximation. Following this approach, the optimal beamforming vectors $\left\{\mathbf{w}_{t,k}^*\right\}_{t\in\mathcal{T},k\in\mathcal{K}}$ can be obtained as described in [46], which can be formulated as

$$\mathbf{w}_{t,k}^* = \left(\mathbf{h}_{t,k}^H \mathbf{V}_{t,k}^* \mathbf{h}_{t,k}\right)^{-1/2} \mathbf{V}_{t,k}^* \mathbf{h}_{t,k}, t \in \mathcal{T}, k \in \mathcal{K}.$$
 (21)

C. Updating APV

To start with, we reformulate constraint (12b) into a more tractable form, i.e.,

$$\frac{\sum_{t=1}^{T} \left| \mathbf{h}_{t,k}^{H} \mathbf{w}_{t,k} \right|^{2}}{\sum_{t=1}^{T} \sum_{k'=1 \atop k' \neq k}^{K'} \left| \mathbf{h}_{t,k}^{H} \mathbf{w}_{t,k'} \right|^{2} + \sigma_{n}^{2}} \ge \Gamma$$

$$\Rightarrow \Gamma^{-1} \sum_{t=1}^{T} \mathbf{h}_{t,k}^{H} \mathbf{V}_{t,k} \mathbf{h}_{t,k} - \sum_{t=1}^{T} \mathbf{h}_{t,k}^{H} \left(\mathbf{V}_{t} - \mathbf{V}_{t,k} \right) \mathbf{h}_{t,k} \ge \sigma_{n}^{2}$$

$$\Rightarrow \sum_{t=1}^{T} \left| \varrho_{t,k} \right|^{2} \mathbf{a}_{1}^{H} \left(\mathbf{p}_{t}, \theta_{t,k} \right) \mathbf{U}_{t,k} \mathbf{a}_{1} \left(\mathbf{p}_{t}, \theta_{t,k} \right) \ge \sigma_{n}^{2}, \quad (22)$$

where

$$\mathbf{U}_{t,k} = (1 + \Gamma^{-1}) \mathbf{V}_{t,k} - \mathbf{V}_t, t \in \mathcal{T}, k \in \mathcal{K}.$$
 (23)

However, the constraint (22) is neither convex nor concave with respect to $\{\mathbf{p}_t\}_{t\in\mathcal{T}}$. To tackle this limitation, we construct a convex surrogate function to locally approximate the original function by adopting the second-order Taylor series expansion, with detailed derivations provided in [23]. Specifically, given a local point $\tilde{\mathbf{p}}_t$, the second-order Taylor expansion of

$$\mathbf{a}_{1}^{H}\left(\mathbf{p}_{t}, \theta_{t,k}\right) \mathbf{U}_{t,k} \mathbf{a}_{1}\left(\mathbf{p}_{t}, \theta_{t,k}\right)$$
 is

$$\mathbf{a}_{1}^{H}\left(\mathbf{p}_{t}, \theta_{t,k}\right) \mathbf{U}_{t,k} \mathbf{a}_{1}\left(\mathbf{p}_{t}, \theta_{t,k}\right) \geq f\left(\mathbf{p}_{t} | \tilde{\mathbf{p}}_{t}\right) = \mathbf{p}_{t}^{T} \mathbf{A}_{t,k} \mathbf{p}_{t} + 2\mathbf{b}_{t,k} \mathbf{p}_{t}^{T} + c_{t,k}. \quad (24)$$

The detailed expressions of $A_{t,k}$, $b_{t,k}$, and $c_{t,k}$ are provided in (25) at the bottom of the next page, where $U_{t,k}$ [m,n] denotes the (m,n)-th element of $U_{t,k}$. Thus, the constraint (22) can be reformulated as

$$\sum_{t=1}^{T} |\varrho_{t,k}|^2 \left(\mathbf{p}_t^T \mathbf{A}_{t,k} \mathbf{p}_t + 2 \mathbf{b}_{t,k} \mathbf{p}_t^T + c_{t,k} \right) \ge \sigma_{\mathrm{n}}^2, k \in \mathcal{K}.$$
 (26)

Subsequently, we extend the Taylor approximation scheme to constraint (18d). For a given local point $\tilde{\mathbf{p}}_t$, the second-order Taylor expansion of $\mathbf{a}_1^H(\mathbf{p}_t, \varphi_{t,r}) \mathbf{V}_t \mathbf{a}_1(\mathbf{p}_t, \varphi_{t,r})$ is

$$\mathbf{a}_{1}^{H}\left(\mathbf{p}_{t}, \varphi_{t,r}\right) \mathbf{V}_{t} \mathbf{a}_{1}\left(\mathbf{p}_{t}, \varphi_{t,r}\right) \geq \mathbf{f}\left(\mathbf{p}_{t} | \tilde{\mathbf{p}}_{t}\right) = \mathbf{p}_{t}^{T} \mathbf{D}_{t,r} \mathbf{p}_{t} + 2\mathbf{e}_{t,r} \mathbf{p}_{t}^{T} + q_{t,r}. \quad (27)$$

The detailed formulas of $\mathbf{D}_{t,r}$, $\mathbf{e}_{t,r}$, and $q_{t,r}$ are provided in (29) at the bottom of the next page, where $\mathbf{V}_t[m,n]$ denotes the (m,n)-th element of \mathbf{V}_t . Through this convexification, the constraint (18d) can be reformulated as

$$\sum_{t=1}^{T} \zeta_{t,r} \left(\mathbf{p}_{t}^{T} \mathbf{D}_{t,r} \mathbf{p}_{t} + 2 \mathbf{e}_{t,r} \mathbf{p}_{t}^{T} + q_{t,r} \right) \ge \xi, r \in \mathcal{R}.$$
 (28)

As such, the resultant optimization problem becomes

$$P_{6}: \max_{\{\mathbf{p}_{t}\}_{t \in \mathcal{T}}, \xi} \xi$$
s.t. (11), (26), (28),

which constitutes a convex quadratically constrained quadratic program (QCQP) that is computationally tractable and can be efficiently solved using CVX.

By adopting the AO algorithm, the details of the proposed algorithm are summarized in **Algorithm** 1^3 , where j_{\max} denotes the maximum number of iterations, j is the iteration index, and μ represents the convergence threshold. Specifically, in step 3, we solve problem P_5 to optimize the beamforming matrices $\{\mathbf{V}_{t,k}\}_{t\in\mathcal{T},k\in\mathcal{K}}$ given the APVs $\{\mathbf{p}_t\}_{t\in\mathcal{T}}$. Subsequently, in step 4, we optimize $\{\mathbf{p}_t\}_{t\in\mathcal{T}}$ by solving problem P_6 with $\{\mathbf{V}_{t,k}\}_{t\in\mathcal{T},k\in\mathcal{K}}$ fixed. The overall algorithm iteratively solves problems P_5 and P_6 within a loop, aiming to asymptotically converge to an optimal solution to P_3 . The initial values for $\{\mathbf{p}_t^{(0)}\}_{t\in\mathcal{T}}$ are calculated by

$$\mathbf{p}_{t}^{(0)} = \left[\frac{D}{M+1}, \frac{2D}{M+1}, \dots, \frac{MD}{M+1} \right], \ t \in \mathcal{T},$$
 (31)

where the positions of the FAs are uniformly spaced with an interval of $\frac{D}{M+1}$ between adjacent elements to minimize mutual coupling effects among them.

 3 The joint optimization problem P_3 is inherently non-convex due to the coupled variables, the non-convex max-min SNR objective function and SINR constraints, as well as the combinatorial aspect introduced by the minimum antenna separation constraint. Consequently, computing the globally optimal solution is computationally intractable for practical system sizes. To address this challenge, the proposed AO algorithm is designed to find a locally optimal solution

Algorithm 1 Alternating Optimization Algorithm.

Input:
$$\{\theta_{t,k}, \varrho_{t,k}\}_{t \in \mathcal{T}, k \in \mathcal{K}}, \{\zeta_{t,r}, \phi_{t,k}\}_{t \in \mathcal{T}, r \in \mathcal{R}}, \{P_t\}_{t \in \mathcal{T}}, D, D_0, \lambda, \sigma_n, \sigma_s, \Gamma, \mu, j_{\max}.$$

Output: $\{\mathbf{w}_{t,k}\}_{t \in \mathcal{T}, k \in \mathcal{K}}, \{\mathbf{p}_t\}_{t \in \mathcal{T}}.$

1: Initialize $\{\mathbf{p}_t^{(0)}\}_{t \in \mathcal{T}}$ according to (31), $\xi^{(0)}$, $\xi^{(1)}$, $j = 1$.

2: for $j \leq j_{\max}$ or $|\xi^{(j)} - \xi^{(j-1)}| \geq \mu$ do

3: Solve problem P_5 with $\{\mathbf{p}_t^{(j-1)}\}_{t \in \mathcal{T}}$ to obtain

3: Solve problem
$$P_5$$
 with $\left\{\mathbf{p}_t^{(j)}\right\}_{t\in\mathcal{T}}$ to obtain $\left\{\mathbf{V}_{t,k}^{(j)}\right\}_{t\in\mathcal{T},k\in\mathcal{K}};$

4: Solve problem
$$P_6$$
 with $\left\{\mathbf{V}_{t,k}^{(j)}\right\}_{t\in\mathcal{T},k\in\mathcal{K}}$ to obtain $\left\{\mathbf{p}_t^{(j)}\right\}_{t\in\mathcal{T}}$ and ξ ;
5: $j\leftarrow j+1$;
6: $\xi^{(j)}\leftarrow \xi$;

- 7: end for
- 8: Obtain $\{\mathbf{w}_{t,k}\}_{t\in\mathcal{T},k\in\mathcal{K}}$ through (21).
- 9: **return** $\{\mathbf{w}_{t,k}\}_{t\in\mathcal{T},k\in\mathcal{K}}$, $\{\mathbf{p}_t\}_{t\in\mathcal{T}}$.

D. Convergence Analysis

Proposition 1. The optimization objective ξ to problem P_3 is non-decreasing throughout the whole iteration process in the proposed AO algorithm, i.e.,

$$\xi\left(\left\{\mathbf{W}_{t}^{(j)}\right\}_{t\in\mathcal{T}}, \left\{\mathbf{p}_{t}^{(j)}\right\}_{t\in\mathcal{T}}\right) \\
\geq \xi\left(\left\{\mathbf{W}_{t}^{(j-1)}\right\}_{t\in\mathcal{T}}, \left\{\mathbf{p}_{t}^{(j-1)}\right\}_{t\in\mathcal{T}}\right), \ j>1. \quad (32)$$

This property ensures that the objective function value monotonically non-decreases with each iteration, thereby ensuring the convergence stability of the proposed algorithm.

E. Complexity Analysis

The computational complexity of the proposed AO algorithm applied to solve problem P_3 is primarily contributed by two main parts: solving problem P_5 for $\{\mathbf{W}_t\}_{t\in\mathcal{T}}$ and solving problem P_6 for $\{\mathbf{p}_t\}_{t\in\mathcal{T}}$. For the first part, it includes TK matrix variables of size $M \times M$, and T + K + R linear constraints. Using interior point methods, this subproblem requires $\mathcal{O}\left(\sqrt{TKM}\log\left(1/\varepsilon\right)\right)$ iterations to converge, where ε is the stopping tolerance. Each iteration requires at most $\mathcal{O}\left(T^3K^3M^6 + TK\left(T + K + R\right)M^2\right)$ [47]. Therefore, the complexity for this part $\mathcal{O}\left(\left(T^{3.5}K^{3.5}M^{6.5} + T^{1.5}K^{1.5}M^{2.5}R\right)\log(1/\varepsilon)\right).$ Similarly, the second part follows a similar pattern but with different parameters. Specifically, the complexity is $\mathcal{O}\left(\left(T^{3.5}M^{3.5} + T^{1.5}M^{1.5}K + T^{1.5}M^{1.5}R\right)\log(1/\varepsilon)\right).$ As a consequence, combining both parts and accounting for the maximum number of iterations j_{max} , the overall computational complexity of the proposed AO algorithm is $\mathcal{O}\left(j_{\max}\left(\left(T^{3.5}K^{3.5}M^{6.5}+T^{1.5}K^{1.5}M^{2.5}R\right)\log\left(1/\varepsilon\right)\right)\right).$

IV. SIMULATION RESULTS

The simulation setup includes the following parameters. The FA-enabled multi-static ISAC system has T=3 TAPs and a RAP, with the locations of the 1-st, 2-nd, 3-rd TAPs, and the RAP being (0,0),

$$\mathbf{A}_{t,k} = -u_{t,k}^{2} \left(\operatorname{diag}(\mathbf{u}_{t,k}) - |\mathbf{U}_{t,k}| \right), \mathbf{b}_{t,k}[n] = u_{t,k}^{2} \sum_{m=1}^{M} \left| \mathbf{U}_{t,k}\left[m,n\right] \right| \left(\tilde{p}_{t,n} - \tilde{p}_{t,m} \right) - u_{t,k} \sum_{m=1}^{M} \left| \mathbf{U}_{t,k}\left[m,n\right] \right| \sin \left(g_{t,k}\left(\tilde{p}_{t,n}, \tilde{p}_{t,m} \right) \right), \quad (25a)$$

$$\mathbf{c}_{t,k} = \sum_{m=1}^{M} \sum_{n=1}^{M} |\mathbf{U}_{t,k}[m,n]| \left[\cos \left(g_{t,k}(\tilde{p}_{t,n}, \tilde{p}_{t,m}) \right) + u_{t,k} \sin \left(g_{t,k}(\tilde{p}_{t,n}, \tilde{p}_{t,m}) \right) (\tilde{p}_{t,n} - \tilde{p}_{t,m}) - \frac{1}{2} u_{t,k}^{2} \left(\tilde{p}_{t,n} - \tilde{p}_{t,m} \right)^{2} \right], \quad (25b)$$

$$u_{t,k} = \frac{2\pi}{\lambda} \sin(\theta_{t,k}), \mathbf{u}_{t,k} = \left[\sum_{m=1}^{M} |\mathbf{U}_{t,k}[m,1]|, \sum_{m=1}^{M} |\mathbf{U}_{t,k}[m,2]|, \dots, \sum_{m=1}^{M} |\mathbf{U}_{t,k}[m,M]| \right],$$
(25c)

$$g_{t,k}\left(\tilde{p}_{t,n},\tilde{p}_{t,m}\right) = u_{t,k}\left(\tilde{p}_{t,n} - \tilde{p}_{t,m}\right) + \angle \mathbf{U}_{t,k}\left[m,n\right]. \tag{25d}$$

$$\mathbf{D}_{t,r} = -\mathfrak{u}_{t,r}^{2} \left(\operatorname{diag} \left(\mathbf{v}_{t} \right) - | \mathbf{V}_{t} | \right), \mathbf{e}_{t,r} \left[n \right] = \mathfrak{u}_{t,r}^{2} \sum_{m=1}^{M} \left| \mathbf{V}_{t} \left[m, n \right] \right| \left(\tilde{p}_{t,n} - \tilde{p}_{t,m} \right) - \mathfrak{u}_{t,r} \sum_{m=1}^{M} \left| \mathbf{V}_{t} \left[m, n \right] \right| \sin \left(\mathfrak{g}_{t,r} \left(\tilde{p}_{t,n}, \tilde{p}_{t,m} \right) \right), \quad (29a)$$

$$\mathbf{q}_{t,r} = \sum_{m=1}^{M} \sum_{n=1}^{M} |\mathbf{V}_{t}[m,n]| \left[\cos \left(\mathbf{g}_{t,r} \left(\tilde{p}_{t,n}, \tilde{p}_{t,m} \right) \right) + \mathbf{u}_{t,r} \sin \left(\mathbf{g}_{t,r} \left(\tilde{p}_{t,n}, \tilde{p}_{t,m} \right) \right) \left(\tilde{p}_{t,n} - \tilde{p}_{t,m} \right) - \frac{1}{2} \mathbf{u}_{t,r}^{2} \left(\tilde{p}_{t,n} - \tilde{p}_{t,m} \right)^{2} \right], \quad (29b)$$

$$\mathfrak{u}_{t,r} = \frac{2\pi}{\lambda} \sin\left(\varphi_{t,r}\right), \mathbf{v}_{t} = \left[\sum_{m=1}^{M} \left|\mathbf{V}_{t}\left[m,1\right]\right|, \sum_{m=1}^{M} \left|\mathbf{V}_{t}\left[m,2\right]\right|, \dots, \sum_{m=1}^{M} \left|\mathbf{V}_{t}\left[m,M\right]\right|\right], \tag{29c}$$

$$\mathfrak{g}_{t,r}\left(\tilde{p}_{t,n},\tilde{p}_{t,m}\right) = \mathfrak{u}_{t,r}\left(\tilde{p}_{t,n} - \tilde{p}_{t,m}\right) + \angle \mathbf{V}_{t}\left[m,n\right]. \tag{29d}$$

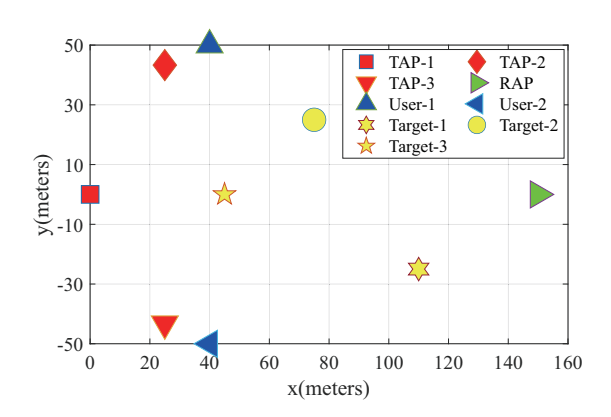


Fig. 3. The 2D locations of the TAPs, RAP, users and the targets.

$\theta_{1,1} = 51.3402^{\circ}$	$\theta_{2,1} = 24.0647^{\circ}$	$\theta_{3,1} = 80.8667^{\circ}$
$\theta_{1,2} = -51.3402^{\circ}$	$\theta_{2,2} = -80.8667^{\circ}$	$\theta_{3,2} = -24.0647^{\circ}$
$\varphi_{1,1} = -12.8043^{\circ}$	$\varphi_{2,1} = -38.7834^{\circ}$	$\varphi_{3,1} = 12.1508^{\circ}$
$\varphi_{1,2} = 18.4349^{\circ}$	$\varphi_{2,2} = -20.1039^{\circ}$	$\varphi_{3,2} = 53.7940^{\circ}$
$\varphi_{1,3} = 0^{\circ}$	$\varphi_{2,3} = -65.2087^{\circ}$	$\varphi_{3,3} = 65.2087^{\circ}$

 $(25\sqrt{3} - 50\sqrt{2}\sin(\pi/12), 50\sqrt{2}\sin(\pi/12) + 25), (25\sqrt{3} 50\sqrt{2}\sin(\pi/12), -50\sqrt{2}\sin(\pi/12) - 25),$ and (150,0), respectively. Additionally, we set K = 2 and R = 3, with positions being (40,50) and (40,-50) for the 1-st and 2-nd users, and (110, -25), (75, 25), and (45, 0) for the 1-st, 2nd, and 3-rd targets. The locations of TAPs, RAP, users, and targets are illustrated in Fig. 3. The RAP is equipped with N=20 receive antennas. In the communication model, we set $\sigma_{\rm n}^2=0$ dBm, and the average channel power gain is given by $\varrho_{t,k} = \omega_t \varpi_{t,k}^{-\eta}$, where ω_t is the average channel power gain, η denotes the pathloss exponents, and $\varpi_{t,k}$ represents the distance between the t-th TAP and the k-th user. For the sensing model, the complex reflection coefficient $\beta_{t,r}$ follows the Swerling-I model [48], suitable for static or slow-moving targets. The FA configuration sets the wavelength $\lambda = 0.01$ m, minimum spacing $D_0 = \lambda/2$, and maximum range $D = M\lambda$ [23], [35]. Furthermore, the angle relationship between TAPs and users/targets are provided in Table II, while the value of $\frac{1}{\|\mathbf{c}_{1,t}-\mathbf{c}_{2,r}\|^2\|\mathbf{c}_0-\mathbf{c}_{2,r}\|^2}$ is detailed in Table III.

A. Performance of FA-enabled Bi-static ISAC System

Firstly, we study an FA-enabled bi-static ISAC system with a single TAP. Based on the aforementioned setup, Fig. 4 characterizes the empirical convergence properties of **Algorithm** 1, where the proposed algorithm achieves stable convergence within 50 iterations. Notably, the monotonic ascent of the objective value validates the effectiveness of our AO framework.

Subsequently, we conducted simulations to investigate the variation of sensing performance (denoted by ξ) with respect to the feasible region D of FAs (expressed in multiples of the wavelength λ) for $M \in \{8,12,16\}$. To quantify beamforming precision, we define the beampattern $\mathfrak{B}(\mathbf{p}_t,\psi)$ at the t-th TAP,

$$\text{Value of } \frac{\text{TABLE III}}{\left\|\mathbf{c}_{1,t} - \mathbf{c}_{2,r}\right\|^2 \left\|\mathbf{c}_{0} - \mathbf{c}_{2,r}\right\|^2}.$$

	r=1	r=2	r = 3
t = 1	0.3532×10^{-7}	0.2560×10^{-7}	0.4479×10^{-7}
t=2	0.3780×10^{-7}	0.5644×10^{-7}	0.3987×10^{-7}
t=3	0.5945×10^{-7}	0.2233×10^{-7}	0.3987×10^{-7}

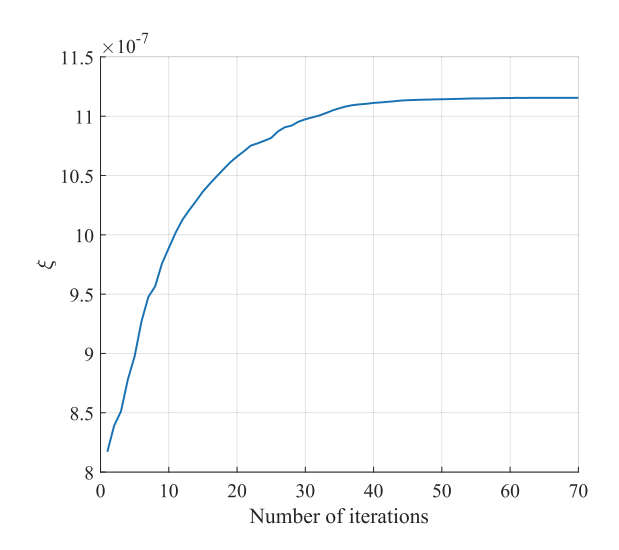


Fig. 4. The convergence performance of the proposed AO algorithm with the first TAP, $M=16,~\Gamma=5$ dB, and $P_1=5$ W.

which is defined as

$$\mathfrak{B}(\mathbf{p}_t, \psi) = \left\| \mathbf{a}_1^H(\mathbf{p}_t, \psi) \mathbf{W}_t \right\|^2, \tag{33}$$

where ψ indicates the steering angle relative to the antenna array. From Fig. 5 (a), we find that the sensing performance ξ monotonically increases with the feasible region D, primarily due to the increased flexibility in optimizing the FA positions within a larger feasible region. As shown in Fig. 5(b), this narrows the beam-width of the main lobe, thereby concentrating energy and improving angular resolution for sensing. Additionally, Figs. 5(a) and (c) reveal that increasing the antenna number can enhance the sensing performance, attributed to higher spatial diversity and array gain. Through joint beamforming optimization, the beam energy can be focused more effectively toward desired directions, further enhancing sensing performance. These results collectively demonstrate that both the FA feasible region and the antenna count are critical factors in achieving superior sensing performance.

To analyze the impact of TAP positions on sensing performance, we show the transmit beampatterns for three different TAPs under varying antenna counts and configuration schemes in Fig. 6. We use the half-wavelength antenna spacing as the baseline scheme, labeled as "HWA". As shown in Fig. 6(a), the first TAP necessitates stronger beam energy allocation for both users to satisfy the minimum SINR requirements. However, the second TAP, being closer to the first user, requires minimal beam energy to satisfy the communication needs for this user, but higher energy for the distant second user, as shown in Fig. 6(b). A similar beam energy allocation pattern applies

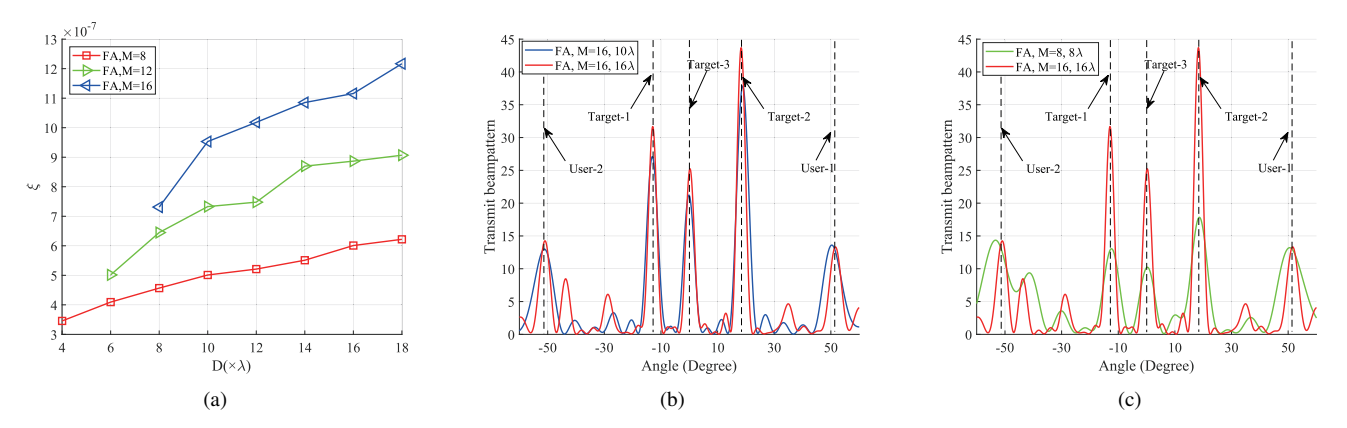


Fig. 5. (a) The performance of sensing versus the feasible region of FAs under different numbers of antennas, (b) and (c) the transmit beampatterns with the first TAP, $\Gamma = 5$ dB, and $P_1 = 5$ W.

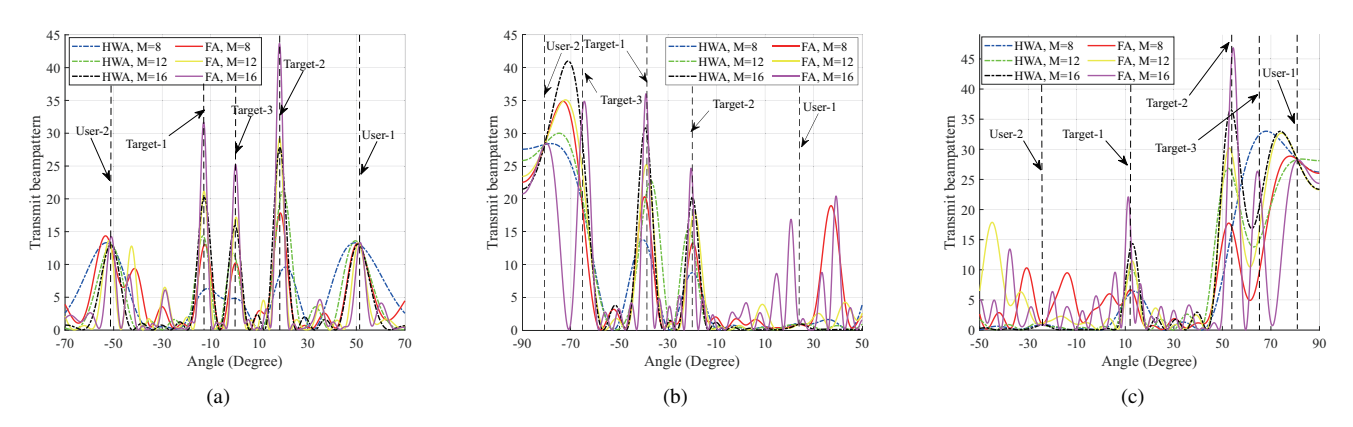


Fig. 6. The transmit beampatterns achieved by (a) the first TAP, (b) the second TAP, (c) the third TAP with $\Gamma=5$ dB, and $P_t=5$ W.

to the third TAP, as depicted in Fig. 6(c). These resource allocation patterns align with the spatial distribution revealed in Fig. 3 and Table II. Additionally, referring to Table III, it is revealed that targets with larger combined path distances (i.e., $\|\mathbf{c}_{1,t} - \mathbf{c}_{2,r}\|^2 \|\mathbf{c}_0 - \mathbf{c}_{2,r}\|^2$) demand increased beam energy to maximize the minimum sensing performance.

Furthermore, as evidenced by Fig. 6, we see that the FA scheme achieves significantly better sensing performance than the baseline scheme, and both the FA and HWA schemes exhibit improved sensing performance with increasing number of antennas. Specifically, under certain conditions, the FA scheme with M=12 achieves superior sensing performance compared to the HWA scheme with M=16 in Fig. 6(a).

However, when the second user and the third target are in close angular proximity, only the FA scheme with M=16 successfully resolves both directions with distinct beam peaks at the second TAP, as shown in Fig. 6(b). In contrast, the HWA scheme with M=16 shows only one beam peak near these angular positions, demonstrating its fundamental limitation in spatial discrimination. This contrast highlights that the FA scheme not only enhances spatial resolution compared to the HWA scheme, but also increases the DoFs through its flexible antenna architecture. Although Fig. 6(c) shows an anomalous case where the HWA scheme with M=8 exhibits a higher beam peak at the third target location compared to

other schemes, this localized enhancement comes at the cost of degraded overall system performance. The apparent peak elevation actually results from the HWA's inadequate spatial resolution at lower antenna counts, causing beam energy dispersion that fails to support multi-target optimization.

B. Performance of FA-enabled Multi-Static ISAC System

Next, we perform a comprehensive evaluation of the sensing capabilities in an FA-enabled multi-static ISAC system. As demonstrated in Figs. 7 and 8, the collaborative sensing mechanism among multiple TAPs reveals significant beam pattern diversity compared to conventional bi-static configurations. Notably, as indicated in Fig. 7, with M=16 antennas, the first and second users' communication requirements are fulfilled by the second and third TAPs, respectively, no matter whether the FA or HWA scheme is employed. This coordinated resource allocation results from the joint optimization of sensing and communication tasks in multi-TAP systems. Specifically, the second and third TAPs allocate more power to satisfy the communication demands of their respective users, taking into account the distance between the users and the TAPs. For sensing performance analysis under the FA scheme, the first TAP primarily generates three distinct beam peaks across different target directions, with the highest peak directed towards the third target. Consequently, the sensing performance for the

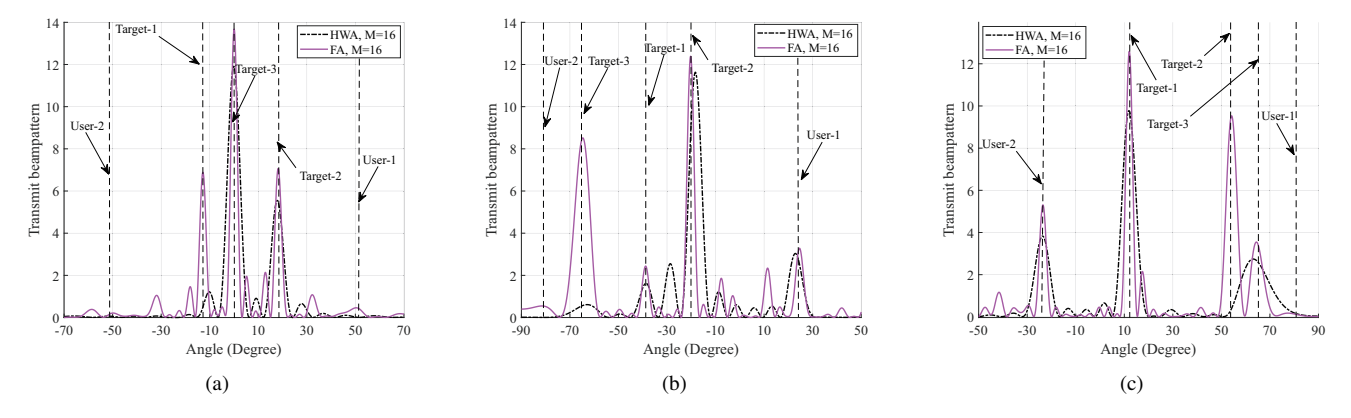


Fig. 7. The transmit beampatterns achieved by (a) the first TAP, (b) the second TAP, (c) the third TAP with $\Gamma=10$ dB, and $P_t=1$ W.

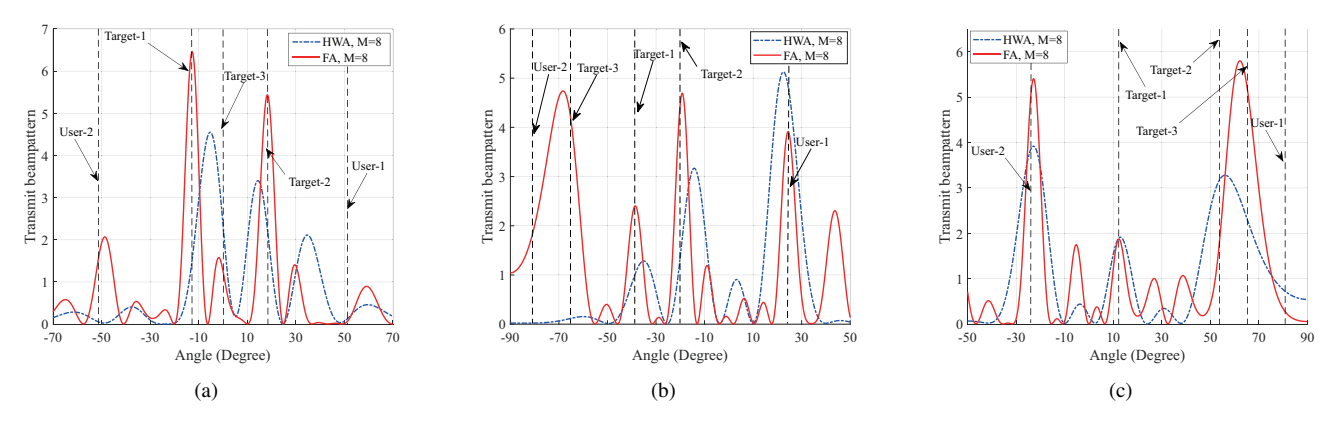


Fig. 8. The transmit beampatterns achieved by (a) the first TAP, (b) the second TAP, (c) the third TAP with $\Gamma=10$ dB, and $P_t=1$ W.

third target is predominantly achieved by the first TAP. The second TAP shows significant peaks for the second and third targets, while the third TAP exhibits notable peaks for the first and second targets.

As a result, the sensing performance for the first and second targets is primarily supported by the third and second TAPs, respectively. These observations are consistent with the comprehensive distance data provided in Table III. In contrast, under the HWA scheme, despite the directions of the maximum beam peaks for each TAP matching those listed in Table III, its fixed-position antennas restrict their ability to narrow the main beam-width and enhance resolution as effectively as the FA scheme. This restriction limits the HWA scheme's ability to achieve beam peaks at closely spaced directions. For instance, as seen in Fig. 7(c), while the FA scheme achieves beam peaks at both second and third targets, HWA only shows one peak at the third target. The FA scheme's adaptability in adjusting its beam pattern enables it to maintain high resolution and performance, even for targets that are closely positioned.

However, when M=8, the beampatterns exhibit distinct trends, as illustrated in Fig. 8. In this configuration, the sensing performance for the third target is not exclusively provided by the first TAP but jointly supported by the second and third TAPs, owing to a comprehensive consideration of system constraints. The decrease in the number of antennas results in diminished spatial resolution, causing the beam peaks for

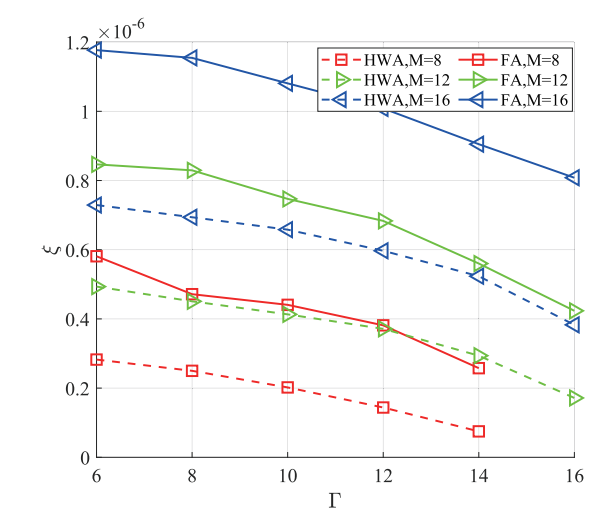
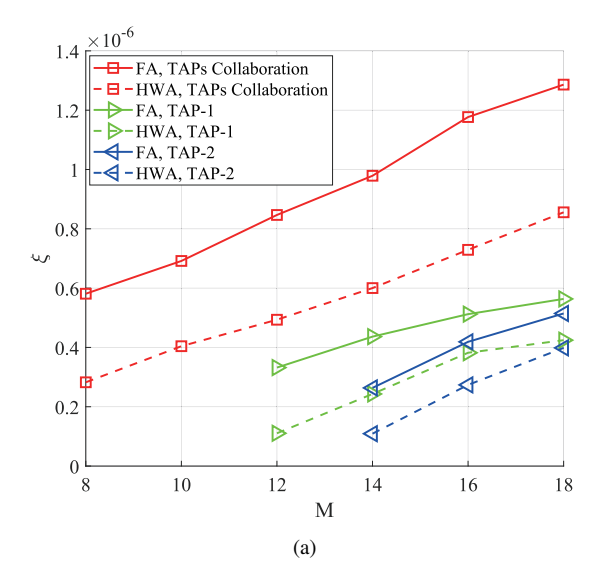


Fig. 9. The performance of sensing versus Γ under different numbers of antennas with $P_t=1$ W.

both targets and users to be less sharply defined compared to M=16. Nevertheless, the FA scheme maintains superior performance compared to the HWA scheme.

Then, Fig. 9 demonstrates the relationship between sensing performance and the user SINR values. The results indicate that sensing performance decreases as the user SINR increases.



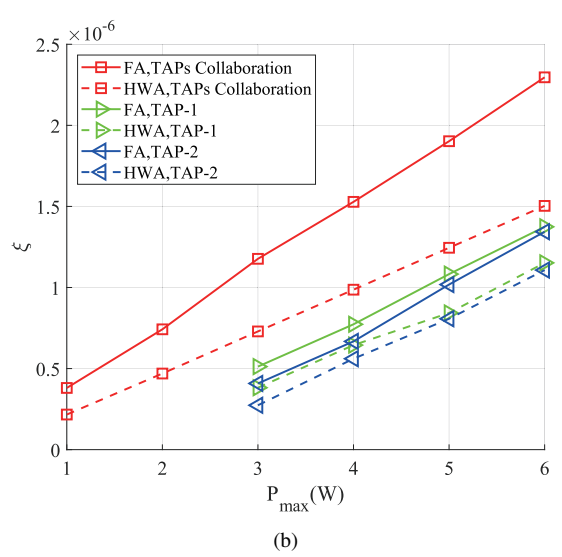


Fig. 10. (a) Performance of sensing versus M with $P_{\rm max}=3$ W and $\Gamma=6$ dB, (b) performance of sensing versus $P_{\rm max}$ with M=16 and $\Gamma=6$ dB.

Specifically, at $\Gamma=16$ dB, none of the configurations with M=8 (for both the FA and HWA schemes) provide a feasible solution. Evidently, the configuration with M=12 using the FA scheme achieves better performance than the one with M=16 using the HWA scheme.

Furthermore, Fig. 10 quantitatively demonstrates the advantages of multi-static ISAC system by contrasting collaborative and standalone setups under various critical system parameters. We begin by introducing the parameter $P_{\rm max}$. In multi-static ISAC system, $P_{\rm max}$ represents the total transmit power across all TAPs, expressed as $P_{\rm max} = \sum_{t=1}^T P_t$. In contrast, for the bi-static ISAC system, $P_{\rm max}$ corresponds to the transmit power of each individual TAP, i.e., $P_{\rm max} = P_t, t \in \mathcal{T}$. This unified definition ensures fair power allocation and enables an equitable performance comparison between the two system architectures. Fig. 10 (a) shows that sensing performance improves with an increased number of antennas across all considered schemes. When operating under the same total transmit power $P_{\rm max}$, the collaborative TAP configuration

achieves superior performance over single-TAP systems by exploiting the spatial diversity offered by distributed TAPs. Notably, although performance differences exist between TAP-1 and TAP-2 in standalone mode, these differences diminish significantly as the number of antennas increases. Further analysis reveals the limitations of bi-static ISAC system. TAP-1 fails to produce feasible solutions when the number of antennas falls below M=12, whereas TAP-2 becomes infeasible at M = 14. This highlights the intrinsic benefit of multi-TAP coordination in mitigating the constraints imposed on individual nodes. Similarly, Fig. 10 (b) illustrates monotonic improvement in sensing performance with increasing total transmit power $P_{\rm max}$ across all schemes. Consistent with the trend observed in Fig. 10 (a), collaborative TAP configurations consistently outperform single-TAP systems under identical antenna settings. Importantly, none of the bi-static schemes meet the required communication constraints at transmit powers below 3 W, highlighting the fundamental power limitations of bi-static systems in the absence of cooperative gains.

V. CONCLUSION

This paper explored an FA-enabled multi-static ISAC system designed to coordinate multi-TAP for collaborative downlink communication and sensing tasks through ISAC signal transmission. A RAP was deployed to capture the reflected sensing signals for target detection. To fully exploit the spatial DoFs provided by the antennas, all TAPs were equipped with FAs. Subsequently, we formulated an optimization problem to maximize the worst-case detection probability for designated targets while satisfying system constraints. To address this non-convex problem, we introduced an AO algorithm that decomposed the problem into two subproblems: optimizing the beamforming matrix and optimizing the APV. For the beamforming matrix optimization, we applied SDR techniques to derive an optimal solution with the fixed APVs. For APV optimization, we adopted a second-order Taylor series expansion to approximate the function of APVs, achieving convexity and determining the optimal antenna positions. Numerical simulations confirmed that the FA scheme significantly enhances the performance of our multi-static ISAC system, substantially outperforming fixed-position configurations. Furthermore, the proposed cooperative multi-static ISAC system demonstrated effective coordination between communication and sensing tasks across different TAPs, highlighting its potential to improve overall system efficiency and performance.

APPENDIX

A. Proof of Proposition 1

In the j-th iteration for solving problem P_5 , the following inequality holds for the objective function:

$$\xi\left(\left\{\mathbf{W}_{t}^{(j)}\right\}_{t\in\mathcal{T}}, \left\{\mathbf{p}_{t}^{(j-1)}\right\}_{t\in\mathcal{T}}\right) \overset{(c_{1})}{\geq}$$

$$\xi\left(\left\{\mathbf{W}_{t}^{(j-1)}\right\}_{t\in\mathcal{T}}, \left\{\mathbf{p}_{t}^{(j-1)}\right\}_{t\in\mathcal{T}}\right), \ j>1, \quad (34)$$

where inequality (c_1) holds because $\xi\left(\left\{\mathbf{W}_t^{(j)}\right\}_{t\in\mathcal{T}}, \left\{\mathbf{p}_t^{(j-1)}\right\}_{t\in\mathcal{T}}\right)$ is maximized in step 3. Similarly, in the j-th iteration for solving problem P_6 , we obtain the following inequality for the objective function:

$$\xi\left(\left\{\mathbf{W}_{t}^{(j)}\right\}_{t\in\mathcal{T}}, \left\{\mathbf{p}_{t}^{(j)}\right\}_{t\in\mathcal{T}}\right) \overset{(c_{2})}{\geq}$$

$$\xi\left(\left\{\mathbf{W}_{t}^{(j)}\right\}_{t\in\mathcal{T}}, \left\{\mathbf{p}_{t}^{(j-1)}\right\}_{t\in\mathcal{T}}\right), \ j>1. \quad (35)$$

where inequality (c_2) is valid since $\xi\left(\left\{\mathbf{W}_t^{(j)}\right\}_{t\in\mathcal{T}}, \left\{\mathbf{p}_t^{(j)}\right\}_{t\in\mathcal{T}}\right)$ is maximized in step 4. Combining both results from (34) and (35), we conclude that

$$\xi\left(\left\{\mathbf{W}_{t}^{(j)}\right\}_{t\in\mathcal{T}}, \left\{\mathbf{p}_{t}^{(j)}\right\}_{t\in\mathcal{T}}\right) \geq \xi\left(\left\{\mathbf{W}_{t}^{(j-1)}\right\}_{t\in\mathcal{T}}, \left\{\mathbf{p}_{t}^{(j-1)}\right\}_{t\in\mathcal{T}}\right), \ j > 1. \quad (36)$$

This implies that the sequence $\left\{\xi\left(\left\{\mathbf{W}_t^{(j)}\right\}_{t\in\mathcal{T}}, \left\{\mathbf{p}_t^{(j)}\right\}_{t\in\mathcal{T}}\right)\right\}_{j=0}^{\infty} \quad \text{is monotonically non-decreasing and converges to its maximum value under the proposed AO framework.}$

REFERENCES

- [1] F. Tariq et al., "A speculative study on 6G," IEEE Wireless Commun., vol. 27, no. 4, pp. 118–125, Aug. 2020.
- [2] W. Chen et al., "5G-advanced toward 6G: Past, present, and future," IEEE J. Sel. Areas Commun., vol. 41, no. 6, pp. 1592–1619, Jun. 2023.
- [3] H. Lu and Y. Zeng, "Communicating with extremely large-scale array/surface: Unified modeling and performance analysis," *IEEE Trans. Wireless Commun.*, vol. 21, no. 6, pp. 4039–4053, Jun. 2022.
- [4] Z. Wang et al., "Extremely large-scale MIMO: Fundamentals, challenges, solutions, and future directions," IEEE Wireless Commun., vol. 31, no. 3, pp. 117–124, Jun. 2024.
- [5] Y. Zeng and X. Xu, "Toward environment-aware 6G communications via channel knowledge map," *IEEE Wireless Commun.*, vol. 28, no. 3, pp. 84–91, Jun. 2021.
- [6] F. Liu, C. Masouros, A. P. Petropulu, H. Griffiths, and L. Hanzo, "Joint radar and communication design: Applications, state-of-the-art, and the road ahead," *IEEE Trans. Commun.*, vol. 68, no. 6, pp. 3834–3862, Jun. 2020
- [7] J. A. Zhang et al., "Enabling joint communication and radar sensing in mobile networks—A survey," *IEEE Commun. Surveys & Tuts.*, vol. 24, no. 1, pp. 306–345, Feb. 2022.
- [8] F. Liu, C. Masouros, A. Li, H. Sun, and L. Hanzo, "MU-MIMO communications with MIMO radar: From co-existence to joint transmission," *IEEE Trans. Wireless Commun.*, vol. 17, no. 4, pp. 2755–2770, Apr. 2018
- [9] X. Liu et al., "Joint transmit beamforming for multiuser MIMO communications and MIMO radar," *IEEE Trans. Signal Process.*, vol. 68, pp. 3929–3944, Jun. 2020.
- [10] H. Hua, J. Xu, and T. X. Han, "Optimal transmit beamforming for integrated sensing and communication," *IEEE Trans. Veh. Technol.*, vol. 72, no. 8, pp. 10588–10603, Aug. 2023.
- [11] C. Dou, N. Huang, Y. Wu, L. Qian, and T. Q. S. Quek, "Sensing-efficient NOMA-aided integrated sensing and communication: A joint sensing scheduling and beamforming optimization," *IEEE Trans. Veh. Technol.*, vol. 72, no. 10, pp. 13591–13603, Oct. 2023.
- [12] J. A. Zhang *et al.*, "Perceptive mobile networks: Cellular networks with radio vision via joint communication and radar sensing," *IEEE Veh. Technol. Mag.*, vol. 16, no. 2, pp. 20–30, Jun. 2021.
- [13] Z. Behdad, Ö. T. Demir, K. W. Sung, E. Björnson, and C. Cavdar, "Multi-static target detection and power allocation for integrated sensing and communication in cell-free massive MIMO," *IEEE Trans. Wireless Commun.*, vol. 23, no. 9, pp. 11580–11596, Apr. 2024.

- [14] X. Lou et al., "Power optimization for integrated active and passive sensing in DFRC systems," *IEEE Trans. Commun.*, vol. 72, no. 6, pp. 3365–3377, Jun. 2024.
- [15] S. Liu, M. Li, and Q. Liu, "Joint BS mode selection and beamforming design for cooperative cell-free ISAC networks," arXiv preprint, arXiv: 2305.10800, 2023.
- [16] R. Li, Z. Xiao, and Y. Zeng, "Toward seamless sensing coverage for cellular multi-static integrated sensing and communication," *IEEE Trans. Wireless Commun.*, vol. 23, no. 6, pp. 5363–5376, Jun. 2024.
- [17] N. Huang et al., "Edge intelligence oriented integrated sensing and communication: A multi-cell cooperative approach," *IEEE Trans. Veh. Technol.*, vol. 73, no. 6, pp. 8810–8824, Jun. 2024.
- [18] H. Gazzah and K. Abed-Meraim, "Optimum ambiguity-free directional and omnidirectional planar antenna arrays for DOA estimation," *IEEE Trans. Signal Process.*, vol. 57, no. 10, pp. 3942–3953, Oct. 2009.
- [19] K. K. Wong, K. F. Tong, Y. Shen, Y. Chen, and Y. Zhang, "Bruce Leeinspired fluid antenna system: Six research topics and the potentials for 6G," Frontiers Commun. and Netw., section Wireless Commun., vol. 3, no. 853416, Mar. 2022.
- [20] W. K. New et al., "A tutorial on fluid antenna system for 6G networks: Encompassing communication theory, optimization methods and hard-ware designs," *IEEE Commun. Surv. & Tut.*, doi:10.1109/COMST.2024. 3498855, 2024.
- [21] K. K. Wong, A. Shojaeifard, K.-F. Tong, and Y. Zhang, "Performance limits of fluid antenna systems," *IEEE Commun. Lett.*, vol. 24, no. 11, pp. 2469–2472, Nov. 2020.
- [22] K. K. Wong, A. Shojaeifard, K.-F. Tong, and Y. Zhang, "Fluid antenna systems," *IEEE Trans. Wireless Commun.*, vol. 20, no. 3, pp. 1950–1962, Mar. 2021.
- [23] W. Ma, L. Zhu, and R. Zhang, "Multi-beam forming with movable-antenna array," *IEEE Commun. Lett.*, vol. 28, no. 3, pp. 697–701, Mar. 2024.
- [24] Z. Chai, K.-K. Wong, K.-F. Tong, Y. Chen, and Y. Zhang, "Port selection for fluid antenna systems," *IEEE Commun. Lett.*, vol. 26, no. 5, pp. 1180–1184, May 2022.
- [25] C. Wang et al., "AI-empowered fluid antenna systems: Opportunities, challenges and future directions," *IEEE Wireless Commun.*, vol. 31, no. 5, pp. 34–41, Oct. 2024.
- [26] W.-J. Lu et al., "Fluid antennas: Reshaping intrinsic properties for flexible radiation characteristics in intelligent wireless networks," accepted in *IEEE Commun. Mag.*, arXiv:2501.02911, 2025.
- [27] J. Zhang et al., "A novel pixel-based reconfigurable antenna applied in fluid antenna systems with high switching speed," *IEEE Open J. Antennas & Propag.*, vol. 6, no. 1, pp. 212–228, Feb. 2025.
- [28] Y. Shen et al., "Design and implementation of mmWave surface wave enabled fluid antennas and experimental results for fluid antenna multiple access," arXiv preprint, arXiv:2405.09663, May 2024.
- [29] R. Wang et al., "Electromagnetically reconfigurable fluid antenna system for wireless communications: Design, modeling, algorithm, fabrication, and experiment," arXiv preprint, arXiv:2502.19643v2, 2025.
- [30] B. Liu, K. F. Tong, K. K. Wong, C.-B. Chae, and H. Wong, "Be water, my antennas: Riding on radio wave fluctuation in nature for spatial multiplexing using programmable meta-fluid antenna," arXiv preprint, arXiv:2502.04693, 2025.
- [31] Z. Li et al., "Movable Antennas Enabled ISAC Systems: Fundamentals, Opportunities, and Future Directions," *IEEE Wireless Commun.*, vol. 1, no. 1, pp. 1-8, Apr. 2025.
- [32] J. Zou et al., "Shifting the ISAC trade-off with fluid antenna systems," IEEE Wireless Commun. Lett., vol. 13, no. 12, pp. 3479–3483, Dec. 2024
- [33] Q. Zhang et al., "An efficient sum-rate maximization algorithm for fluid antenna-assisted ISAC system," *IEEE Commun. Lett.*, vol. 29, no. 1, pp. 200–204, Jan. 2025.
- [34] T. Hao et al., "Fluid-antenna enhanced ISAC: Joint antenna positioning and dual-functional beamforming design under perfect and imperfect CSI," arXiv preprint, arXiv:2407.18988, 2024.
- [35] L. Zhou, J. Yao, M. Jin, T. Wu, and K.-K. Wong, "Fluid antenna-assisted ISAC systems," *IEEE Commun. Lett.*, vol. 13, no. 12, pp. 3533–3537, Dec. 2024.
- [36] H. Wu, H. Ren, C. Pan, and Y. Zhang, "Movable antenna-enabled RISaided integrated sensing and communication," arXiv preprint, arXiv: 2407.03228, 2024.
- [37] C. Wang et al., "Fluid antenna system liberating multiuser MIMO for ISAC via deep reinforcement learning," *IEEE Trans. Wireless Commun.*, vol. 23, no. 9, pp. 10879–10894, Sept. 2024.
- [38] E. G. Larsson, "Massive synchrony in distributed antenna systems," IEEE Trans. Signal Process., vol. 72, pp. 855–866, Jan. 2024.

- [39] H. Godrich, A. M. Haimovich, and R. S. Blum, "Target localization accuracy gain in MIMO radar-based systems," *IEEE Trans. Inf. Theory*, vol. 56, no. 6, pp. 2783–2803, May 2010.
 [40] F. Liu *et al.*, "Cramér-rao bound optimization for joint radar-
- [40] F. Liu et al., "Cramér-rao bound optimization for joint radar-communication beamforming," *IEEE Trans. Signal Process.*, vol. 70, pp. 240–253, Feb. 2022.
- [41] X. Lou, W. Xia, S. Jin, and H. Zhu, "Beamforming optimization in distributed ISAC system with integrated active and passive sensing," *IEEE Trans. Commun.*, vol. 73, no. 3, pp. 1607–1620, Mar. 2025.
- [42] R. Li et al., "IRS Aided Millimeter-Wave Sensing and Communication: Beam Scanning, Beam Splitting, and Performance Analysis," IEEE Trans. Wireless Commun., vol. 23, no. 12, pp. 19713-19727, Dec. 2024.
- [43] L. Zhu et al., "Movable antennas for wireless communication: Opportunities and challenges," *IEEE Commun. Mag.*, vol. 62, no. 6, pp. 114-120, Jun. 2024.
- [44] S. Boyd, S. P. Boyd, and L. Vandenberghe, *Convex optimization*. Cambridge University Press, 2004.
- [45] Z.-Q. Luo, W.-K. Ma, A. M.-C. So, Y. Ye, and S. Zhang, "Semidefinite relaxation of quadratic optimization problems," *IEEE Signal Process. Mag.*, vol. 27, no. 3, pp. 20–34, May 2010.
- [46] X. Liu et al., "Joint transmit beamforming for multiuser MIMO communications and MIMO radar," *IEEE Trans. Signal Process.*, vol. 68, pp. 3929–3944, Jun. 2020.
- [47] E. Karipidis, N. D. Sidiropoulos, and Z.-Q. Luo, "Quality of service and max-min fair transmit beamforming to multiple cochannel multicast groups," *IEEE Trans. Signal Process.*, vol. 56, no. 3, pp. 1268–1279, Mar. 2008.
- [48] J. L. Eaves and E. K. Reedy, Principles of Modern Radar. New York: Van Nostrand Reinhold, 1987.